

Quench Dynamics of a Fermi Gas with Strong Long-Range Interactions

Elmer Guardado-Sánchez,¹ Benjamin M. Spar,¹ Peter Schauss,² Ron Belyansky,^{3,4} Jeremy T. Young,^{3,5} Przemysław Bienias,^{3,4} Alexey V. Gorshkov,^{3,4} Thomas Iadecola,⁶ and Waseem S. Bakr^{1,*}

¹*Department of Physics, Princeton University, Princeton, New Jersey 08544 USA*

²*Department of Physics, University of Virginia, Charlottesville, Virginia 22904 USA*

³*Joint Quantum Institute, NIST/University of Maryland, College Park, Maryland 20742, USA*

⁴*Joint Center for Quantum Information and Computer Science,*

NIST/University of Maryland, College Park, Maryland 20742 USA

⁵*JILA, NIST and Department of Physics, University of Colorado, Boulder, CO 80309, USA*

⁶*Department of Physics and Astronomy, Iowa State University, Ames, Iowa 50011, USA*

(Dated: June 4, 2022)

We induce strong non-local interactions in a 2D Fermi gas in an optical lattice using Rydberg dressing. The system is approximately described by a $t - V$ model on a square lattice where the fermions experience isotropic nearest-neighbor interactions and are free to hop only along one direction. We measure the interactions using many-body Ramsey interferometry and study the lifetime of the gas in the presence of tunneling, finding that tunneling does not reduce the lifetime. To probe the interplay of non-local interactions with tunneling, we investigate the short-time relaxation dynamics of charge density waves in the gas. We find that strong nearest-neighbor interactions slow down the relaxation. Our work opens the door for quantum simulations of systems with strong non-local interactions such as extended Fermi-Hubbard models.

Ultracold gases are a versatile platform for studying quantum many-body physics [1]. The ability to engineer and control the interactions in these systems has played an important role in observing novel phases of matter including crossover fermionic superfluids [2] and dipolar supersolids [3–5] and in studying out-of-equilibrium dynamical processes such as thermalization [6]. Recent efforts have focused on degenerate quantum gases with long-range interactions including those of magnetic atoms [3, 6–8] and polar molecules [9, 10]. These systems may be distinguished from other quantum platforms with long-range interactions including ions [11, 12], Rydberg atoms [13], polar molecules in optical tweezers [14, 15] and atoms in optical cavities [16], in that the particles are itinerant. This can lead to an interesting interplay between interactions, kinetic energy and quantum statistics. Rydberg dressing has been proposed as an alternative route to realize quantum gases with tunable long-range interactions [17–19]. Experimental demonstrations of Rydberg dressing [20–29] have been performed with localized atoms or quantum gases of heavy atoms where observation of motional effects has been elusive. Here we investigate Rydberg dressing of lithium-6, a light fermionic atom. Its fast tunneling in an optical lattice allows us to study the quench dynamics of itinerant fermions with strong, purely off-site interactions.

Atoms in a quantum gas resonantly coupled to a Rydberg state experience strong van der Waals interactions many orders of magnitude larger than their kinetic energy for typical interatomic spacings, hindering access to the interesting regime where the two energy scales compete. At the same time, the population of atoms in the

Rydberg state decays on a timescale of tens of microseconds, short compared to millisecond motional timescales. Rydberg dressing addresses both of these issues. Using an off-resonant coupling, the atoms are prepared in a laser-dressed eigenstate $|g_{\text{dr}}\rangle \approx |g\rangle + \beta|r\rangle$ of predominant ground state ($|g\rangle$) character and a small Rydberg ($|r\rangle$) admixture, where $\beta = \frac{\Omega}{2\Delta} \ll 1$, Ω is the coupling strength, and Δ is the laser detuning from the transition frequency. This enhances the lifetime of the dressed atom by a factor of $1/\beta^2$ relative to the bare Rydberg state lifetime. On the other hand, the interaction between two atoms a distance r apart is reduced in strength and can be approximately described by a tunable softcore potential $V(r) = V_{\text{max}}/(r^6 + r_c^6)$ with strength $V_{\text{max}} \sim \beta^3\Omega$ and range $r_c \sim (|C_6/2\Delta|)^{1/6}$, where C_6 is the van der Waals coefficient for the Rydberg-Rydberg interaction. Early experiments with 3D quantum gases were limited by rapid collective atom loss attributed to a blackbody-induced avalanche dephasing effect [20–22, 26]. Nevertheless, Rydberg dressing has been successfully used to entangle atoms in optical tweezers [23], perform electrometry in bulk gases [28], and study spin dynamics [24, 27, 29].

In this work, we report on the single-photon Rydberg dressing of a 2D ${}^6\text{Li}$ Fermi gas in an optical lattice in the presence of tunneling. This results in a lattice gas of fermions with strong, non-local interactions. We characterize the interaction potential using many-body Ramsey interferometry [24]. A careful study of the lifetime of spin-polarized gases shows different behavior compared to previous Rydberg dressing realizations, with the lifetime depending strongly on the density but not on the atom number at fixed density. We also observe that the presence of tunneling in the system has no effect on the lifetime. Finally, we use this platform to realize a $t - V$ model consisting of interaction-coupled chains and study

* Corresponding author. Email: wbakr@princeton.edu

the short-time quench dynamics of charge-density wave states, finding that the strong attractive interactions inhibit the motion of the atoms.

Our system consists of a degenerate Fermi gas of ${}^6\text{Li}$ atoms in a square optical lattice of spacing $a_{\text{latt}} = 752\text{ nm}$ (Fig. 1a) [31]. We apply a 592 G magnetic field perpendicular to the 2D system. We load spin-polarized gases prepared in a state that may be labeled at high fields as $|nl, m_l, m_s, m_I\rangle = |2S, 0, -1/2, 1\rangle = |1\rangle$, or alternatively $|2S, 0, -1/2, -1\rangle = |3\rangle$ depending on the measurement. We have control over the initial density profile by em-

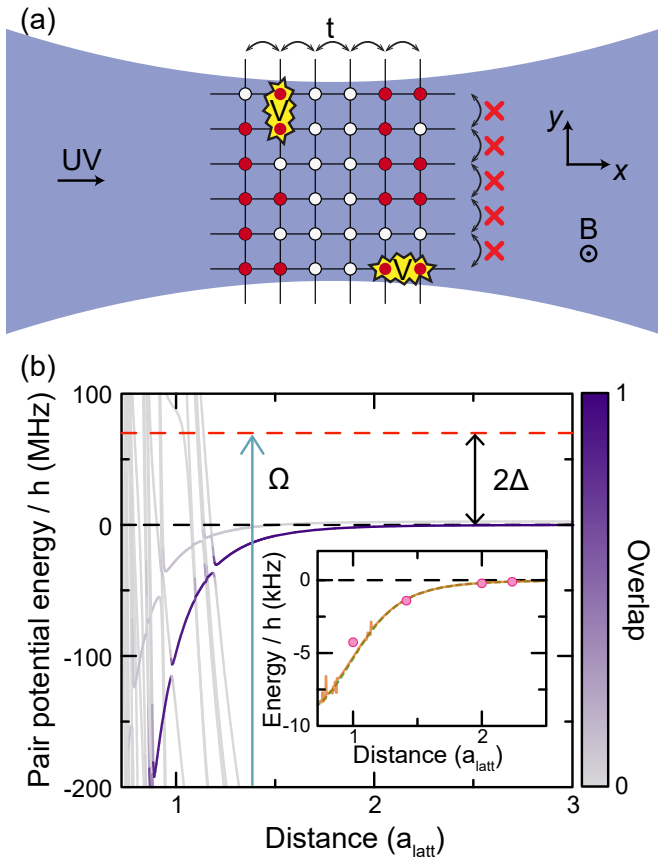


FIG. 1. Realization of a $t - V$ model with Rydberg dressing. (a) The Rydberg dressing beam propagates along the x -direction of the lattice, effectively decoupling 1D chains in the y -direction due to a differential light shift. Hopping of fermions (red dots) along the x -direction is unaffected. Interactions are isotropic. (b) ${}^6\text{Li}$ pair potentials for dressing to the state $|28P, m_l = 0, m_s = -1/2\rangle$ calculated using [30]. The color of the lines represents the overlap with the target pair-state ($|28P, 0, -1/2\rangle \otimes |28P, 0, -1/2\rangle$) coupled via the laser with Rabi coupling Ω and detuning Δ from the target state. Inset: Calculated dressed potential for $\Omega = 2\pi \times 7.7\text{ MHz}$ and $\Delta = 2\pi \times 35\text{ MHz}$ taking into account the overlaps to all pair potentials (orange solid line). The dashed green line represents the expected dressed potential for a simple van der Waals potential with $C_6 = h \times 90\text{ MHz } a_{\text{latt}}^6$. Pink points are the interaction at each lattice distance taking into account the wavefunction spread of the atoms.

ploying a spatial light modulator. Using a 231 nm laser beam with linear polarization parallel to the magnetic field and propagating along the lattice x -direction, we couple the ground state atoms to the $|28P, 0, -1/2\rangle$ Rydberg state [32]. By tuning the intensity and the detuning of the dressing light, we have real-time control over the isotropic soft-core interaction potential between the atoms in the gas (Fig. 1b).

The lattice system is described by a single-band spinless fermion Hamiltonian

$$\hat{H} = -t \sum_{\langle i,j \rangle} (\hat{c}_i^\dagger \hat{c}_j + \text{h.c.}) + \sum_{i \neq j} V_{ij} \hat{n}_i \hat{n}_j + \sum_i \delta_i \hat{n}_i, \quad (1)$$

where t is a tunneling matrix element, V_{ij} is the off-site interaction and δ_i is the potential due to single-particle light shifts contributed by the lattice and Rydberg dressing beams. Since our dressing beam is tightly focused with a waist of $\sim 16\text{ }\mu\text{m}$, the change in δ between rows in the y -direction, which is orthogonal to the beam propagation axis, is much larger than t . On the other hand, because of the large Rayleigh range of the beam ($\sim 3.5\text{ mm}$), the variation of δ along the beam propagation direction (x -direction) is negligible. To first approximation, we drop the light shift term and the hopping along the y -direction. Thus, we can rewrite our Hamiltonian as a coupled-chain $t - V$ model of the form

$$\hat{H} = -t \sum_{\langle i,j \rangle_x} (\hat{c}_i^\dagger \hat{c}_j + \text{h.c.}) + \sum_{i \neq j} V_{ij} \hat{n}_i \hat{n}_j. \quad (2)$$

In order to characterize the long-range interaction potentials, we perform many-body Ramsey interferometry between states $|1\rangle$ and $|2\rangle = |2S, 0, -1/2, 0\rangle$ following the procedure introduced in Ref. [24]. Starting from a spin-polarized band insulator of atoms prepared in state $|1\rangle$ in a deep lattice that suppresses tunneling, a $\pi/2$ radiofrequency pulse prepares a superposition of state $|1\rangle$ and $|2\rangle$, which acquire a differential phase during a subsequent evolution for time T in the presence of the dressing light. Unlike Ref. [24], the splitting between the hyperfine ground-states of ${}^6\text{Li}$ is comparable to the detuning Δ of the dressing laser (Fig. 2a), and both states are significantly dressed by the light [32]. First, we obtain the spatial profile of the Rabi coupling strength $\Omega(i, j)$ by measuring the population of $|2\rangle$ after a $\pi/2 - T - \pi/2$ pulse sequence using a detuning $\Delta = 2\pi \times 100\text{ MHz}$. The large detuning is chosen so that the interactions, whose strength scales as $1/\Delta^3$, are negligible, while the single-particle light shifts that scale as $1/\Delta$ lead to a large differential phase during the evolution. From these measurements, we extract the waist of the beam ($16.1(4)\text{ }\mu\text{m}$) and measure Rabi couplings up to $\Omega = 2\pi \times 9.5\text{ MHz}$ (Fig. 2b). The measured spatial profile of the Ramsey fringe frequency confirms the rapid variation of δ_i along the y -direction, while no variation of δ_i is observed along the x -direction within the statistical uncertainty of the measurement ($\sim 1\text{ kHz}$).

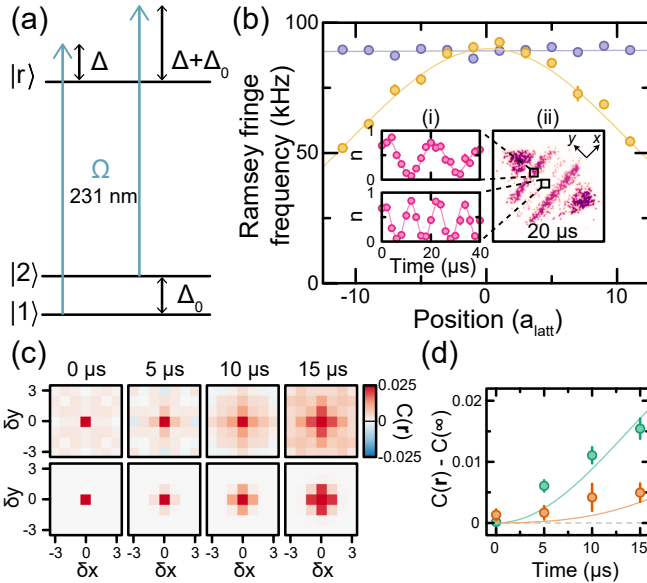


FIG. 2. Measuring Rydberg dressed interactions with many-body Ramsey interferometry. (a) Energy level diagram for ${}^6\text{Li}$ showing that the dressing of the other hyperfine ground state cannot be ignored. Here $\Delta/2\pi$ is varied between 30 and 100 MHz while $\Delta_0/2\pi = 76$ MHz. (b) Ramsey fringe frequency measured at a detuning of $\Delta = 2\pi \times 100$ MHz at different positions in the cloud. The frequency is almost constant along the propagation direction of the beam (purple). In the transverse direction (yellow), it varies rapidly as expected for a tightly focused Gaussian beam. Insets: (i) Ramsey oscillations at two representative positions in the cloud. (ii) Sample image of one spin state in the cloud at $T = 20$ μs . (c) Spin correlations for different spin-echo pulse times at $\Omega = 2\pi \times 7.7$ MHz and $\Delta = 2\pi \times 35$ MHz. Measurement (top) and theoretical expectation (bottom) [32]. (d) Nearest (orange) and next-nearest (green) neighbor correlations after subtracting $C(\infty)$. Lines correspond to the expected correlations.

To probe interactions in the system, we switch to a smaller detuning $\Delta = 2\pi \times 35$ MHz. We measure density correlations of state $|1\rangle$ ($C(\mathbf{r}) = \langle n_1(\mathbf{r})n_1(0) \rangle - \langle n_1(\mathbf{r}) \rangle \langle n_1(0) \rangle$) after a spin-echo pulse sequence ($\pi/2 - T - \pi - T - \pi/2$) which eliminates differential phases due to the light shift. Fig. 2c shows the measured correlations after different evolution times T compared to the theoretical expectation [32]. Fig. 2d depicts the evolution of the nearest-neighbor and next-nearest-neighbor correlations with the correlation offset $C(\infty)$ subtracted. This offset is attributed to correlated atom number fluctuations in the images [24]. We find good agreement with the theoretical model, which predicts a nearest-neighbor (next-nearest-neighbor) attractive interaction $|V_{10}| = h \times 4.3$ kHz ($V_{11} = h \times 1.2$ kHz) (Fig. 1b)

To probe coherent many-body physics in our system, the lifetime τ of the sample has to be larger than the interaction and tunneling times. Atoms resonantly excited to a Rydberg state are lost from our system on a timescale of tens of microseconds for several reasons:

photon recoils due to spontaneous emission and large forces due to anti-trapping optical potentials and due to interactions with other Rydberg atoms. Due to its Rydberg admixture, an isolated dressed atom decays with a lifetime $\tau_{\text{eff}} = \tau_0/\beta^2$, where τ_0 is the lifetime of the Rydberg state determined by radiative and blackbody-driven transitions to other states. Previous experiments with frozen 2D and 3D systems have observed much shorter lifetimes than τ_{eff} [20–22, 24, 26]. A simplified model used to explain these experiments considers a blackbody-driven decay of the dressed state to a pure Rydberg state of opposite parity. The first such contaminant appears in the system on a timescale $\tau_c = \tau_{\text{BB}}/(N\beta^2)$ where τ_{BB} is the blackbody lifetime of the Rydberg state and N is the number of atoms in the system. This atom interacts with other dressed atoms through resonant state-exchange characterized by a C_3 coefficient, broadening the Rydberg line. In particular, other atoms at a certain facilitation radius ($|C_3/\Delta|^{1/3}$) will be resonantly excited, leading to avalanche loss of all the atoms from the trap. Experiments in 2D have indeed observed a collective lifetime close to τ_c and a bimodal atom number distribution in lifetime measurements [24]. We have not observed such bimodality in our 2D systems, and the lifetime does not depend strongly on N at fixed density [32]. In this regard, our 2D ${}^6\text{Li}$ experiments are closer to ${}^{87}\text{Rb}$ experiments with 1D chains where the avalanche mechanism is suppressed to some extent [27].

The atom number decay in a frozen system of 7 by 7 sites is shown in Fig. 3a. The decay is not exponential, indicating a density-dependent lifetime which we extract by fitting different sections of the decay curve. For dressing to $|28P\rangle$, $\tau_0 = 30.5$ μs [33]. We measured the density-dependent lifetime for $\Omega = 2\pi \times 9.25$ MHz at three different detunings, $\Delta = 2\pi \times (30, 40, 60)$ MHz (Fig. 3b). Around half-filling, the collective lifetime is $\sim 0.3\tau_{\text{eff}}$ for $\Delta = 2\pi \times 30$ MHz and approaches τ_{eff} for the smallest densities ($n \sim 0.1$). For comparison, perfect avalanche loss would predict $\tau_c = 0.08\tau_{\text{eff}}$.

Next, we measure the lifetime of the dressed gas in the presence of tunneling, which has been a topic of theoretical debate [34, 35]. We measure the density-dependent lifetime for different lattice depths, spanning the frozen gas regime to a tunneling of 1.7 kHz (Fig. 3c). We do not observe any change of the lifetime with tunneling. A potential concern in this measurement is that the tunneling along the x -direction may be suppressed by uncontrolled disorder in δ_i . We rule this out by preparing a sparse strip of atoms and observing its tunneling dynamics. As expected for a clean dressed system, the tunneling dynamics along the x -direction is almost identical to the case without the dressing light, while the dynamics is frozen along the y -direction (Fig. 3c inset). Combining the results of our interferometry and lifetime measurements, we achieve a lifetime of several interaction times measured by the figure of merit $2\pi V_{10}\tau \sim 20$ for a mobile system with $n = 0.5$.

To probe the interplay of interactions and tunneling in

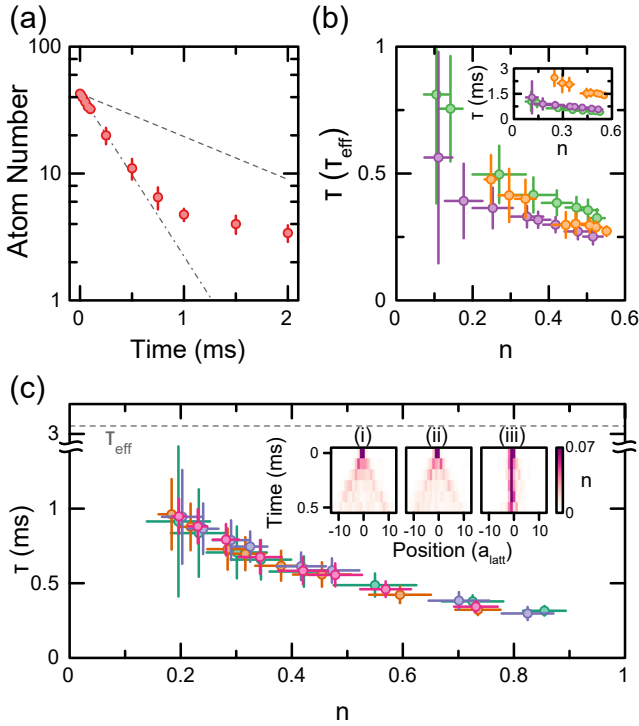


FIG. 3. **Lifetime of itinerant Rydberg dressed fermions.** (a) Atom number vs. dressing time for a frozen gas. The red circles correspond to measurements on a system of 7 by 7 sites. Dashed-dotted line corresponds to an exponential fit to the first 5 data points and dashed line corresponds to the expected single-particle dressed lifetime τ_{eff} . (b) Measured lifetime in a frozen gas in units of τ_{eff} vs. the initial density for $\Omega = 2\pi \times 9.25 \text{ MHz}$ and $\Delta = 2\pi \times (30 \text{ (green)}, 40 \text{ (purple)}, 60 \text{ (orange)}) \text{ MHz}$. Inset: Same measurements in units of ms. (c) Lifetime vs. initial density for different tunnelings: 0.01 kHz (green), 0.25 kHz (purple), 1.0 kHz (orange), and 1.7 kHz (pink). The data is taken with $\Omega = 2\pi \times 6.0 \text{ MHz}$, $\Delta = 2\pi \times 30 \text{ MHz}$. Insets: (i) Tunneling dynamics of atoms sparsely initialized on a strip along the y -direction with no dressing light. From this data, we extract a tunneling rate $t = h \times 1.7 \text{ kHz}$. (ii) Same measurement in the presence of the dressing light. (iii) Same measurement in the presence of the dressing light but with the strip along the x -direction.

our system, we use light patterned with a spatial light modulator to initialize the system in a charge density wave state of atoms in state $|3\rangle$. The initial density pattern approximates a square wave with period $\lambda = 4 a_{\text{latt}}$ and width $w = 7 a_{\text{latt}}$, with the average density oscillating between $n \sim 0$ and $n \sim 0.7$. (see Figs. 4a-b). Dynamics in a lattice with $t = h \times 1.7 \text{ kHz}$ is initiated by suddenly turning off the patterning potential while keeping walls in the y -direction as in [36]. We average the density profiles over the non-hopping direction and observe a qualitative change in the dynamics as we increase V/t (here $V \equiv |V_{10}|$) from 0 to 2.9 (Fig. 4c). To emphasize the evolution of the pattern, we scale the data to account for atom loss during the evolution [32]. In the

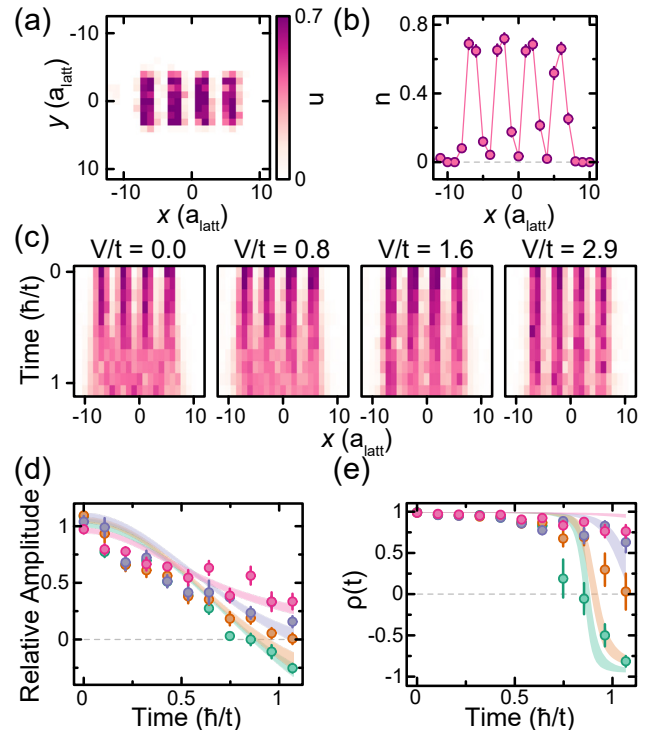


FIG. 4. **Interaction dependence of quench dynamics of a charge density wave.** (a) Average initial state density profile for the quench measurements. (b) Density profile averaged along the y -direction of the initial state shown in (a). (c) Density profile time evolution for interactions $V/t = [0, 0.8, 1.6, 2.9]$. Color scale is the same as in (a). (d) Fitted relative amplitude of density profile vs. time. Colors (green, orange, purple, and pink) correspond to the interactions in (c) from lowest to highest. (e) Autocorrelation function of the density pattern. Colors are same as in (d). Shaded curves correspond to numerical simulations.

non-interacting quench, we observe that the phase of the charge density wave inverts at a time $\sim \hbar/t$ as is expected for a coherent evolution [37]. For strong interactions, the decay of the charge density wave slows down and the system retains a memory of its initial state for longer times. If longer range interactions are ignored, this can be understood to be a result of the conservation of the number of “bonds” between nearest-neighbor atoms in the limit $t/V \rightarrow 0$. In particular, states of the form “11001100...” along the hopping direction, which the imprinted density pattern attempts to approximate, are dynamically frozen in that limit [38].

To quantify the difference in the dynamics of the different quenches, we employ two different methods. The first is to fit a sinusoid of the form $n(x, t) = A \sin(2\pi x/\lambda + \phi) + B$ to determine the amplitude of the wave relative to its mean, A/B (Fig. 4d). The fit is restricted to $|x| \leq 6 a_{\text{latt}}$, and ϕ is fixed by the initial pattern. The second method is to calculate the autocor-

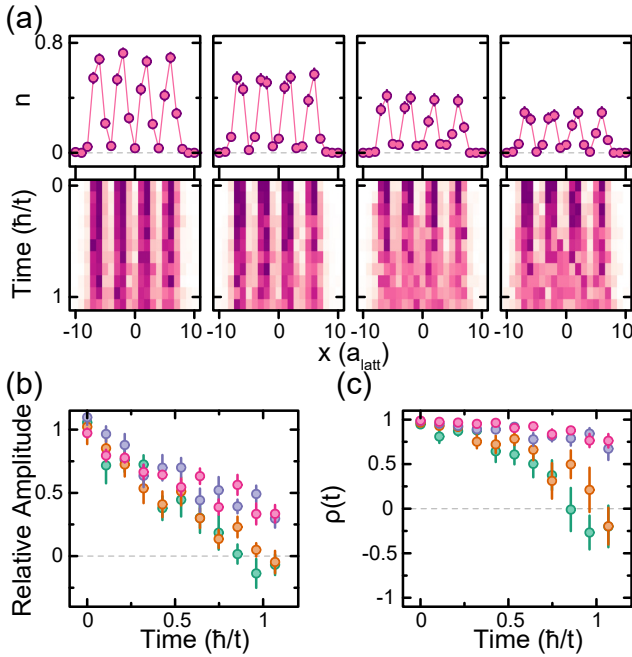


FIG. 5. Density dependence of quench dynamics. (a) (top) Initial state density profiles. (bottom) Corresponding time evolution of each initial state for $V/t = 2.9$. (b) Fitted relative amplitude of density profiles vs. time. Colors (green, orange, purple, and pink) correspond to the initial states in (a) from low to high density. (c) Autocorrelation function of the density pattern. Colors are same as in (b).

relation function

$$\rho(t) = \frac{\text{cov}_x(n(x, 0), n(x, t))}{\sigma_x(n(x, 0))\sigma_x(n(x, t))}, \quad (3)$$

where cov_x and σ_x are the covariance and the standard deviation respectively (Fig. 4e). Since exact classical simulations of the dynamics of the full 2D Hamiltonian (Eq. 1) are computationally intractable, we compare instead to numerics on a 2×11 $t - V$ model with only nearest-neighbor interactions and no tunneling along the y -direction and find qualitative agreement with the measurements. We do not account for atom loss in these numerics. The agreement is not as good for a 1D system of comparable length [32]. This points to the importance of taking interchain interactions into account, which slow down the decay of the waves further.

Further confirmation that the slower decay of the charge density waves is an interaction effect is obtained by varying the average density in the initial state. Fig. 5 shows these initial states and their time evolution for $V/t = 2.9$. As the average density of the initial state is decreased, it approaches a “sparse” limit where the probability of having two neighboring atoms is negligible. In this regime, the system is effectively non-interacting

and we recover the phase inversion during the evolution. Since these measurements are done at fixed power of the dressing light, they rule out disorder-induced localization as a mechanism for arresting the dynamics.

Our results present a new frontier in quantum simulations of itinerant lattice models with strong off-site interactions. For example, spinless fermion models may be used to study equilibrium phases such as topological Mott states [39] or cluster Luttinger liquid phases [40] as well as non-equilibrium physics related to prethermalization [41] and Hilbert-space fragmentation [42]. The close spacing between the hyperfine ground states of ${}^6\text{Li}$ also opens the door for the simultaneous dressing of two spin states and the exploration of extended Fermi-Hubbard models. While the current interaction-lifetime figure of merit has allowed us to start exploring coherent dynamics in our system, there are several possible approaches to improve it. Enhancement of the Rabi coupling by over an order of magnitude may be achieved using a build-up cavity [43]. For a single-particle system, the figure of merit scales with Ω at fixed β , while further enhancement of the collective lifetime is expected in this regime due to shrinking facilitation radii for increasing Δ . The principal quantum number used in this experiment was chosen to keep the range of the interaction on the order of one site. Relaxing this constraint or alternatively using larger lattice spacings would allow using longer-lived Rydberg states at higher principal quantum number. Using electric fields to tune close to a Förster resonance results in deep potential wells that may be exploited to enhance the figure of merit by a factor of $|\Delta|/\Omega$ [44]. Finally, collective black-body induced atom loss may be completely eliminated by operating at cryogenic temperatures.

ACKNOWLEDGMENTS

We thank David Huse and Alan Morningstar for helpful discussions. We also thank Zoe Yan, Adam Kaufman and Ana Maria Rey for feedback on the manuscript. This work was supported by the NSF (grant no. DMR-1607277), the David and Lucile Packard Foundation (grant no. 2016-65128), and the AFOSR Young Investigator Research Program (grant no. FA9550-16-1-0269). W.S.B. was supported by an Alfred P. Sloan Foundation fellowship. R.B., J.T.Y., P.B., and A.V.G. acknowledge funding by AFOSR, AFOSR MURI, DoE ASCR Quantum Testbed Pathfinder program (award No. DE-SC0019040), U.S. Department of Energy Award No. DE-SC0019449, DoE ASCR Accelerated Research in Quantum Computing program (award No. DE-SC0020312), NSF PFCQC program, ARL CDQI, ARO MURI, and NSF PFC at JQI. R.B. was also supported by fellowships from the NSERC and FRQNT of Canada. J.T.Y was supported in part by the NIST NRC Research Postdoctoral Associateship Award.

- [1] I. Bloch, J. Dalibard, and W. Zwerger, “Many-body physics with ultracold gases,” *Rev. Mod. Phys.* **80**, 885–964 (2008).
- [2] M. Inguscio, W. Ketterle, and C. Salomon, eds., *Ultracold Fermi Gases, Proceedings of the International School of Physics Enrico Fermi, Course CLXIV, Varenna 2006* (IOS Press, Amsterdam, 2008).
- [3] F. Böttcher, J.-N. Schmidt, M. Wenzel, J. Hertkorn, M. Guo, T. Langen, and T. Pfau, “Transient supersolid properties in an array of dipolar quantum droplets,” *Phys. Rev. X* **9**, 011051 (2019).
- [4] L. Tanzi, E. Lucioni, F. Famà, J. Catani, A. Fioretti, C. Gabbanini, R. N. Bisset, L. Santos, and G. Modugno, “Observation of a dipolar quantum gas with metastable supersolid properties,” *Phys. Rev. Lett.* **122**, 130405 (2019).
- [5] L. Chomaz, D. Petter, P. Ilzhöfer, G. Natale, A. Trautmann, C. Politi, G. Durastante, R. M. W. van Bijnen, A. Patscheider, M. Sohmen, M. J. Mark, and F. Ferlaino, “Long-lived and transient supersolid behaviors in dipolar quantum gases,” *Phys. Rev. X* **9**, 021012 (2019).
- [6] Y. Tang, W. Kao, K.-Y. Li, S. Seo, K. Mallayya, M. Rigol, S. Gopalakrishnan, and B. L. Lev, “Thermalization near integrability in a dipolar quantum newton’s cradle,” *Phys. Rev. X* **8**, 021030 (2018).
- [7] A. Patscheider, B. Zhu, L. Chomaz, D. Petter, S. Baier, A.-M. Rey, F. Ferlaino, and M. J. Mark, “Controlling dipolar exchange interactions in a dense three-dimensional array of large-spin fermions,” *Phys. Rev. Research* **2**, 023050 (2020).
- [8] L. Gabardos, B. Zhu, S. Lepoutre, A. M. Rey, B. Laburthe-Tolra, and L. Vernac, “Relaxation of the collective magnetization of a dense 3D array of interacting dipolar $s = 3$ atoms,” *Phys. Rev. Lett.* **125**, 143401 (2020).
- [9] L. De Marco, G. Valtolina, K. Matsuda, W. G. Tobias, J. P. Covey, and J. Ye, “A degenerate Fermi gas of polar molecules,” *Science* **363**, 853–856 (2019).
- [10] J. L. Bohn, A. M. Rey, and J. Ye, “Cold molecules: Progress in quantum engineering of chemistry and quantum matter,” *Science* **357**, 1002–1010 (2017).
- [11] R. Blatt and C. F. Roos, “Quantum simulations with trapped ions,” *Nat. Phys.* **8**, 277–284 (2012).
- [12] C. D. Bruzewicz, J. Chiaverini, R. McConnell, and J. M. Sage, “Trapped-ion quantum computing: Progress and challenges,” *Appl. Phys. Rev.* **6**, 021314 (2019).
- [13] M. Saffman, T. G. Walker, and K. Mølmer, “Quantum information with Rydberg atoms,” *Rev. Mod. Phys.* **82**, 2313–2363 (2010).
- [14] L. Anderegg, L. W. Cheuk, Y. Bao, S. Burchesky, W. Ketterle, K.-K. Ni, and J. M. Doyle, “An optical tweezer array of ultracold molecules,” *Science* **365**, 1156–1158 (2019).
- [15] L. R. Liu, J. D. Hood, Y. Yu, J. T. Zhang, K. Wang, Y.-W. Lin, T. Rosenband, and K.-K. Ni, “Molecular assembly of ground-state cooled single atoms,” *Phys. Rev. X* **9**, 021039 (2019).
- [16] H. Ritsch, P. Domokos, F. Brennecke, and T. Esslinger, “Cold atoms in cavity-generated dynamical optical potentials,” *Rev. Mod. Phys.* **85**, 553–601 (2013).
- [17] G. Pupillo, A. Micheli, M. Boninsegni, I. Lesanovsky, and P. Zoller, “Strongly correlated gases of Rydberg-dressed atoms: Quantum and classical dynamics,” *Phys. Rev. Lett.* **104**, 223002 (2010).
- [18] J. E. Johnson and S. L. Rolston, “Interactions between Rydberg-dressed atoms,” *Phys. Rev. A* **82**, 033412 (2010).
- [19] N. Henkel, R. Nath, and T. Pohl, “Three-dimensional roton excitations and supersolid formation in Rydberg-excited Bose-Einstein condensates,” *Phys. Rev. Lett.* **104**, 195302 (2010).
- [20] J. B. Balewski, A. T. Krupp, A. Gaj, S. Hofferberth, R. Löw, and T. Pfau, “Rydberg dressing: understanding of collective many-body effects and implications for experiments,” *New J. Phys.* **16**, 063012 (2014).
- [21] E. A. Goldschmidt, T. Boulier, R. C. Brown, S. B. Koller, J. T. Young, A. V. Gorshkov, S. L. Rolston, and J. V. Porto, “Anomalous broadening in driven dissipative Rydberg systems,” *Phys. Rev. Lett.* **116**, 113001 (2016).
- [22] J. A. Aman, B. J. DeSalvo, F. B. Dunning, T. C. Killian, S. Yoshida, and J. Burgdörfer, “Trap losses induced by near-resonant Rydberg dressing of cold atomic gases,” *Phys. Rev. A* **93**, 043425 (2016).
- [23] Y.-Y. Jau, A. M. Hankin, T. Keating, I. H. Deutsch, and G. W. Biedermann, “Entangling atomic spins with a Rydberg-dressed spin-flip blockade,” *Nat. Phys.* **12**, 71–74 (2016).
- [24] J. Zeiher, R. van Bijnen, P. Schauß, S. Hild, J.-Y. Choi, T. Pohl, I. Bloch, and C. Gross, “Many-body interferometry of a Rydberg-dressed spin lattice,” *Nat. Phys.* **12**, 1095–1099 (2016).
- [25] C. Gaul, B. J. DeSalvo, J. A. Aman, F. B. Dunning, T. C. Killian, and T. Pohl, “Resonant Rydberg dressing of alkaline-earth atoms via electromagnetically induced transparency,” *Phys. Rev. Lett.* **116**, 243001 (2016).
- [26] T. Boulier, E. Magnan, C. Bracamontes, J. Maslek, E. A. Goldschmidt, J. T. Young, A. V. Gorshkov, S. L. Rolston, and J. V. Porto, “Spontaneous avalanche dephasing in large Rydberg ensembles,” *Phys. Rev. A* **96**, 053409 (2017).
- [27] J. Zeiher, J.-Y. Choi, A. Rubio-Abadal, T. Pohl, R. van Bijnen, I. Bloch, and C. Gross, “Coherent many-body spin dynamics in a long-range interacting Ising chain,” *Phys. Rev. X* **7**, 041063 (2017).
- [28] A. Arias, G. Lochead, T. M. Wintermantel, S. Helmrich, and S. Whitlock, “Realization of a Rydberg-dressed Ramsey interferometer and electrometer,” *Phys. Rev. Lett.* **122**, 053601 (2019).
- [29] V. Borish, O. Marković, J. A. Hines, S. V. Rajagopal, and M. Schleier-Smith, “Transverse-field Ising dynamics in a Rydberg-dressed atomic gas,” *Phys. Rev. Lett.* **124**, 063601 (2020).
- [30] S. Weber, C. Tresp, H. Menke, A. Urvoy, O. Firstenberg, H. P. Büchler, and S. Hofferberth, “Tutorial: Calculation of Rydberg interaction potentials,” *J. Phys. B: At. Mol. Opt. Phys.* **50**, 133001 (2017).
- [31] E. Guardado-Sánchez, P. T. Brown, D. Mitra, T. Devakul, D. A. Huse, P. Schauß, and W. S. Bakr, “Probing the quench dynamics of antiferromagnetic correlations in a 2D quantum Ising spin system,” *Phys. Rev. X* **8**, 021069 (2018).
- [32] See the Supplemental Material.

- [33] I. I. Beterov, I. I. Ryabtsev, D. B. Tretyakov, and V. M. Entin, “Quasiclassical calculations of blackbody-radiation-induced depopulation rates and effective lifetimes of Rydberg nS , nP , and nD alkali-metal atoms with $n \leq 80$,” *Phys. Rev. A* **79**, 052504 (2009).
- [34] W. Li, C. Ates, and I. Lesanovsky, “Nonadiabatic motional effects and dissipative blockade for Rydberg atoms excited from optical lattices or microtraps,” *Phys. Rev. Lett.* **110**, 213005 (2013).
- [35] T. Macrì and T. Pohl, “Rydberg dressing of atoms in optical lattices,” *Phys. Rev. A* **89**, 011402 (2014).
- [36] E. Guardado-Sánchez, A. Morningstar, B. M. Spar, P. T. Brown, D. A. Huse, and W. S. Bakr, “Subdiffusion and heat transport in a tilted two-dimensional Fermi-Hubbard system,” *Phys. Rev. X* **10**, 011042 (2020).
- [37] P. T. Brown, D. Mitra, E. Guardado-Sánchez, R. Nourafkan, A. Reymbaut, C.-D. Hébert, S. Bergeron, A.-M. S. Tremblay, J. Kokalj, D. A. Huse, P. Schauß, and W. S. Bakr, “Bad metallic transport in a cold atom Fermi-Hubbard system,” *Science* **363**, 379–382 (2019).
- [38] G. De Tomasi, D. Hetterich, P. Sala, and F. Pollmann, “Dynamics of strongly interacting systems: From Fock-space fragmentation to many-body localization,” *Phys. Rev. B* **100**, 214313 (2019).
- [39] A. Dauphin, M. Müller, and M. A. Martin-Delgado, “Rydberg-atom quantum simulation and Chern-number characterization of a topological Mott insulator,” *Phys. Rev. A* **86**, 053618 (2012).
- [40] M. Mattioli, M. Dalmonte, W. Lechner, and G. Pupillo, “Cluster Luttinger liquids of Rydberg-dressed atoms in optical lattices,” *Phys. Rev. Lett.* **111**, 165302 (2013).
- [41] N. Nesi, A. Iucci, and M. A. Cazalilla, “Quantum quench and prethermalization dynamics in a two-dimensional Fermi gas with long-range interactions,” *Phys. Rev. Lett.* **113**, 210402 (2014).
- [42] T. Rakovszky, P. Sala, R. Verresen, M. Knap, and F. Pollmann, “Statistical localization: From strong fragmentation to strong edge modes,” *Phys. Rev. B* **101**, 125126 (2020).
- [43] S. F. Cooper, Z. Burkley, A. D. Brandt, C. Rasor, and D. C. Yost, “Cavity-enhanced deep ultraviolet laser for two-photon cooling of atomic hydrogen,” *Opt. Lett.* **43**, 1375–1378 (2018).
- [44] R. M. W. van Bijnen and T. Pohl, “Quantum magnetism and topological ordering via Rydberg dressing near Förster resonances,” *Phys. Rev. Lett.* **114**, 243002 (2015).
- [45] P. T. Brown, D. Mitra, E. Guardado-Sánchez, P. Schauß, S. S. Kondov, E. Khatami, T. Paiva, N. Trivedi, D. A. Huse, and W. S. Bakr, “Spin-imbalance in a 2D Fermi-Hubbard system,” *Science* **357**, 1385–1388 (2017).

SUPPLEMENTAL MATERIAL

The experimental setup and basic parameters are described in detail in the supplement of Ref. [45]. The procedure for calibrating the spatial light modulator is described in the supplement of Ref [37]. The 231 nm UV laser system for Rydberg excitation is described in the supplement of Ref. [31]. In section I of this supplement, we describe upgrades to the UV laser system to improve its power stability that were crucial for the many-body Ramsey interferometry experiments. In sections II, III and IV, we discuss how to take into account the significant dressing of *both* states involved in the interferometry. In sections V and VI, we provide additional measurements related to the lifetime of Rydberg dressed gases. Finally, in section VII, we provide details on the numerical simulations of the $t - V$ model used to describe the experiment.

I. Power stabilization of the Rydberg dressing light

The UV light used for Rydberg dressing is generated using a 923 nm amplified diode laser system followed by two second harmonic generation cavities in series. The fractional power stability of the UV light after the second cavity is about 10% which was sufficient for our previous work with direct excitation to Rydberg states [31]. However, in the case of dressing, power stability is more critical due to the interaction strength having a quartic dependence on the Rabi frequency ($V \propto \Omega^4$). Furthermore, the stability of the power during the spin-echo sequence used in the Ramsey interferometry is important to cancel the phases accumulated due to the single-particle light shift. We improved the power stability to much better than 1% by adding a noise-eater. The noise-eater consists of an electro-optic polarization modulator (QuBig PCx2B-UV) and an α -BBO Glan-Taylor polarizer (EKSMA 441-2108). By measuring the laser power using a pick-off before the last acousto-optic modulator ([31]) and feeding back on the noise-eater, we suppressed intensity noise for frequencies up to 1 MHz and eliminated shot-to-shot drifts in the dressing light intensity that limited our previous experiments.

II. Ground and Rydberg states used in the experiments

We work at a magnetic field of 592 G pointing in the direction perpendicular to the 2D lattice plane. At this field, both the ground and Rydberg states are in the Paschen-Back regime such that we can approximately label them using the $|nl, m_l, m_s, m_I\rangle$ basis (Fig. S1a). As explained in the text, the hyperfine ground states we use are $|1\rangle$, $|2\rangle$ and $|3\rangle$ numbered from lowest to highest in energy and having $m_I = 1, 0, -1$ respectively. For the Rydberg states, the nuclear spin splitting is negligible so states with different m_I can be considered degenerate. This approximation means that

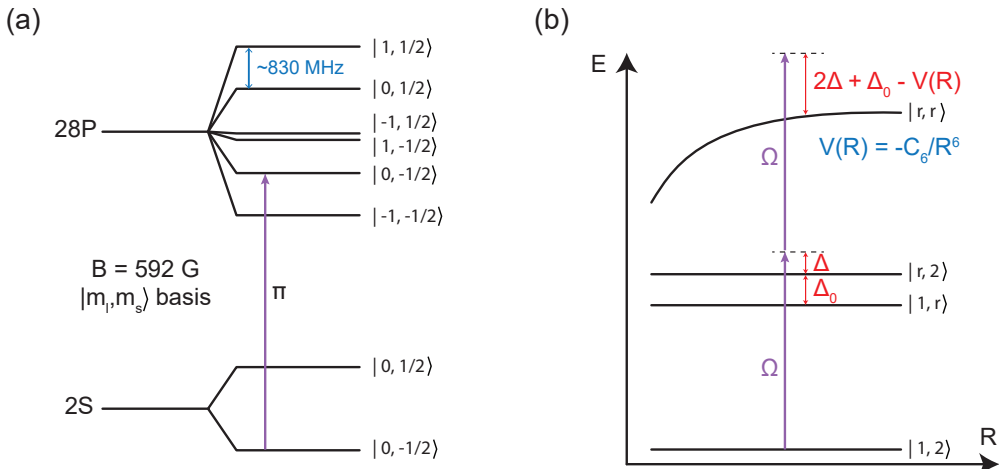


FIG. S1. Rydberg dressing of ^6Li . (a) Level diagram showing the hyperfine ground states of ^6Li directly coupled to the $28P$ Rydberg state using linearly (π) polarized light at a field of 592 G. The basis used is $|m_l, m_s\rangle$. (b) Rydberg dressing scheme for two atoms in different hyperfine ground states $|1\rangle$ and $|2\rangle$ coupled to the Rydberg state $|r\rangle$. Ω is the Rabi coupling of the laser, Δ is the detuning from the resonant transition between $|1\rangle$ and $|r\rangle$, Δ_0 is the hyperfine splitting between $|1\rangle$ and $|2\rangle$ and $V(R) = -C_6/R^6$ is the van der Waals interaction potential between two Rydberg states $|r\rangle$.

two atoms in different hyperfine ground states will couple to Rydberg states at the same energy (both labeled as $|r\rangle$) and interact with each other via a van der Waals potential (Fig. S1b).

In our quenches and lifetime measurements, we always start with a spin-polarized gas of either state $|1\rangle$ or $|3\rangle$ atoms (both states are essentially equivalent and we happen to have taken some of our data in this paper using one or the other). However, for the interferometry measurements, we need to take into account the dressed interaction potential between two atoms in different hyperfine ground states which couple to $|r\rangle$.

III. Interaction potential for two Rydberg dressed atoms in different ground states

To obtain the dressed potential for two atoms in different ground states, we start by writing down the single-particle Hamiltonians for each atom in the $\{|i\rangle, |r\rangle\}$ basis in the rotating frame (where $i \in \{1, 2\}$ labels the ground states):

$$\hat{H}_1 = \begin{pmatrix} 0 & \Omega/2 \\ \Omega/2 & -\Delta \end{pmatrix} \quad \text{and} \quad \hat{H}_2 = \begin{pmatrix} 0 & \Omega/2 \\ \Omega/2 & -(\Delta + \Delta_0) \end{pmatrix}. \quad (\text{S1})$$

Using these and the interaction potential between two atoms in the Rydberg state separated by a distance R , $V(R) = -C_6/R^6$, we write down the two-particle dressing Hamiltonian as

$$\hat{H}_{\text{dr}}(R) = \hat{H}_1 \otimes \hat{\mathbb{I}} + \hat{\mathbb{I}} \otimes \hat{H}_2 + V(R)(|r\rangle\langle r| \otimes |r\rangle\langle r|). \quad (\text{S2})$$

We calculate the dressed potential by solving for the eigenenergy of the eigenstate with maximum overlap with the bare ground state $|1, 2\rangle$. This can be done numerically, or using perturbation theory up to 4th order in Ω assuming $\Omega \ll \Delta$. In this limit, we find that the relevant eigenenergy has the form

$$E(R) = -\frac{\Omega^4(2\Delta + \Delta_0)}{16\Delta^2(\Delta + \Delta_0)^2} \left(\frac{1}{1 + \frac{(2\Delta + \Delta_0)R^6}{|C_6|}} \right) + \delta(\Omega, \Delta) + \delta(\Omega, \Delta + \Delta_0), \quad (\text{S3})$$

where $\delta(\Omega, \Delta) = (-\Delta + \sqrt{\Delta^2 + \Omega^2})/2$ is the single-particle light shift and the first term is the desired interaction potential.

IV. Many-body Ramsey interferometry

We use the same many-body Ramsey interferometry technique as Ref. [24] to characterize the interaction potentials of the Rydberg dressed atoms. However, because the splitting between the ground states we use in the Ramsey interferometry is only ~ 76 MHz and the detunings we use are between 30 and 100 MHz, we need to take into account the dressing of both states. Since the experiments are performed in the frozen-gas regime, we rewrite the dressing Hamiltonian as a spin Hamiltonian. For our interferometer, we use hyperfine ground states $|1\rangle \equiv |\uparrow\rangle$ and $|2\rangle \equiv |\downarrow\rangle$. The many-body dressing Hamiltonian is

$$\hat{H}_{\text{dr}} = \sum_i \left(\delta_i^\uparrow \hat{\sigma}_{\uparrow\uparrow}^{(i)} + \delta_i^\downarrow \hat{\sigma}_{\downarrow\downarrow}^{(i)} \right) + \frac{1}{2} \sum_{i \neq j} \left(V_{ij}^{\uparrow\uparrow} \hat{\sigma}_{\uparrow\uparrow}^{(i)} \hat{\sigma}_{\uparrow\uparrow}^{(j)} + V_{ij}^{\downarrow\downarrow} \hat{\sigma}_{\downarrow\downarrow}^{(i)} \hat{\sigma}_{\downarrow\downarrow}^{(j)} + V_{ij}^{\uparrow\downarrow} \hat{\sigma}_{\uparrow\uparrow}^{(i)} \hat{\sigma}_{\downarrow\downarrow}^{(j)} + V_{ij}^{\downarrow\uparrow} \hat{\sigma}_{\downarrow\downarrow}^{(i)} \hat{\sigma}_{\uparrow\uparrow}^{(j)} \right), \quad (\text{S4})$$

where δ_i^α is the single-particle light shift for spin α at site i , $V_{ij}^{\alpha\beta}$ is the Rydberg dressed potential between spins α and β at sites i and j , and $V_{ij}^{\uparrow\downarrow} = V_{ij}^{\downarrow\uparrow}$. Using the relations $\hat{\sigma}_{\uparrow\uparrow}^{(i)} = \frac{1}{2} (\hat{\mathbb{I}} + \hat{\sigma}_z^{(i)})$ and $\hat{\sigma}_{\downarrow\downarrow}^{(i)} = \frac{1}{2} (\hat{\mathbb{I}} - \hat{\sigma}_z^{(i)})$, we can rewrite the Hamiltonian as

$$\hat{H}_{\text{dr}} = H_0 + \frac{1}{2} \sum_i \left(\delta_i^\uparrow - \delta_i^\downarrow + \frac{1}{2} \sum_{j \neq i} (V_{ij}^{\uparrow\uparrow} - V_{ij}^{\downarrow\downarrow}) \right) \hat{\sigma}_z^{(i)} + \frac{1}{8} \sum_{i \neq j} (V_{ij}^{\uparrow\uparrow} + V_{ij}^{\downarrow\downarrow} - 2V_{ij}^{\uparrow\downarrow}) \hat{\sigma}_z^{(i)} \hat{\sigma}_z^{(j)} \quad (\text{S5})$$

$$= H_0 + \frac{1}{2} \sum_i \delta_i^* \hat{\sigma}_z^{(i)} + \frac{1}{8} \sum_{i \neq j} V_{ij}^* \hat{\sigma}_z^{(i)} \hat{\sigma}_z^{(j)}, \quad (\text{S6})$$

where H_0 is an energy offset, the second term is a longitudinal field of strength δ_i^* dominated by the single-particle light shifts, and the third term is an effective interaction term with strength V_{ij}^* . Similar to what is done in the

supplement of Ref. [24], we can calculate various observables for different pulse sequences in terms of the accumulated phases $\phi_i = \int_0^\tau \delta_i^*(t)dt$ and $\Phi_{ij} = \int_0^\tau V_{ij}^*(t)dt$ over the length τ of the dressing pulse.

For a $\pi/2 - \tau - \pi/2$ pulse sequence, the observable is the expected single-component density $\hat{\sigma}_{\uparrow\uparrow}^i = |\uparrow\rangle\langle\uparrow|$ which can be calculated to be:

$$\langle \hat{\sigma}_{\uparrow\uparrow}^i \rangle = \frac{1}{2} - \frac{1}{2} \cos(\phi_i) \prod_{j \neq i} \cos\left(\frac{\Phi_{ij}}{2}\right). \quad (\text{S7})$$

For a spin echo $\pi/2 - \tau - \pi - \tau - \pi/2$ pulse sequence, the observable is the single-component density correlation which can be calculated to be:

$$\langle \hat{\sigma}_{\uparrow\uparrow}^i \hat{\sigma}_{\uparrow\uparrow}^j \rangle_C = \frac{1}{8} \left(\prod_{k \neq i,j} \cos \Phi_{k,ij}^{(+)} + \prod_{k \neq i,j} \cos \Phi_{k,ij}^{(-)} \right) - \frac{1}{4} \cos \Phi_{ij}^2 \prod_{k \neq i,j} \cos \Phi_{ik} \cos \Phi_{jk}, \quad (\text{S8})$$

where $\Phi_{k,ij}^{(\pm)} = \Phi_{ik} \pm \Phi_{jk}$ and $\Phi_{ii} = 0$.

V. Dependence of lifetime on atom number at fixed density

In our search for a suitable Rydberg state to use for our dressing experiments, we explored many different principal quantum numbers. We eventually chose $28P$ because it gave us a good ratio between the measured collective lifetime and the theoretical single-particle lifetime, while also having a large enough C_6 to achieve strong nearest-neighbor interactions in the lattice. We explored larger principal quantum numbers but found much shorter lifetimes than the expected values. One possible reason is the coupling to neighboring pair-potentials that have non-zero overlaps with the target state at close distances (Fig. 1). However, the general behavior of the many-body lifetimes with atom number and geometry of the cloud remained the same over significantly different principal quantum numbers. In particular, the lifetime showed no strong dependence on the atom number at fixed density over the range we could explore in the experiment. Fig. S2 shows the initial lifetime vs. the initial atom number for 2D systems $4 a_{\text{latt}}$ wide and of variable length along the direction parallel to the dressing beam for the $31P$ and $40P$ Rydberg states.

VI. Atom loss during charge density wave dynamics

We observe an atom loss of $\sim 30\%$ for the longest evolution times for the dataset with the maximum initial density and interaction strength. For the dataset where interaction was varied by changing the dressing laser intensity, the

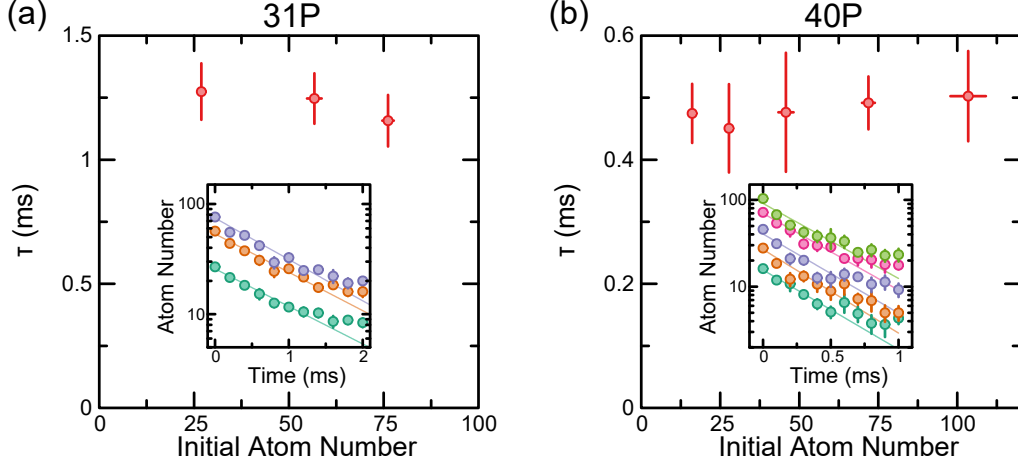


FIG. S2. **Dependence of lifetime on atom number at fixed density.** (a) Initial lifetime for 2D systems with different initial atom number dressed to $31P$. Measurements are made in a 2D rectangular system of small width $\sim 4 a_{\text{latt}}$ and variable length along the dressing beam direction. We observe no strong dependence on the atom number. The Rabi frequency is approximately constant over the entire system. For this data, $\Omega = 2\pi \times 6.9$ MHz, $\Delta = 2\pi \times 60$ MHz and $n = 0.8$. (b) Same as in (a) but for systems dressed to $40P$. For this data, $\Omega = 2\pi \times 5.6$ MHz, $\Delta = 2\pi \times 40$ MHz and $n = 0.55$. (insets) Raw data with exponential fits to extract the initial decay rate.

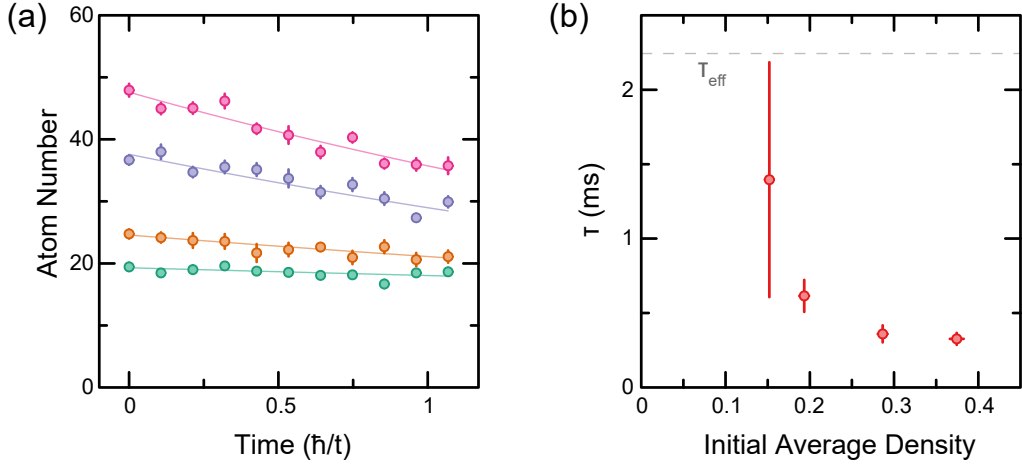


FIG. S3. **Atom loss during charge density wave dynamics.** (a) Atom number decay over the quenches shown in Fig. 5. Each color represents a set with a different initial density. Circles are measured data with s.e.m. errorbars and lines are simple exponential decay fits. The dressing parameters were $\Omega = 2\pi \times 7$ MHz and $\Delta = 2\pi \times 30$ MHz. (b) Lifetime vs. the initial average density of the charge density wave as extracted from the data in (a). This behavior is in agreement with our observations shown in Fig. 3.

lifetime gets longer for smaller interactions due to the reduction of the Rydberg dressing parameter $\beta = \frac{\Omega}{2\Delta}$. For the dataset where the initial density was varied at fixed interaction strength, the lifetime increased for lower initial densities (Fig. S3). These measurements are in accordance with our observed density dependent lifetime measurements shown in Fig. 3.

VII. Numerical simulations

We use exact diagonalization to simulate the quench dynamics of our experiment. Since tunneling along the vertical direction can be neglected, the fermionic $t-V$ model used in the main text to approximately describe the experiment is equivalent, via the Jordan-Wigner transformation, to an XXZ spin model with only nearest-neighbor interactions. As the simulation for the full experimental 2D system ($\sim 7 \times 21$) is computationally intractable, we limit our calculations to 2×11 systems.

The initial state is sampled directly from the experimental data taken at $t = 0$. We pick a 2×9 region centered on 2 of the 4 density peaks from the experimental images (Fig. 4a). In order to reduce boundary effects, we add empty sites on each end of the chain. We average the resulting dynamics over the different sampled initial states, whose number is comparable to the number of experimental snapshots. Next, we analyze the averaged simulated dynamics using the same methods we use for the experimental data. Fig. 4 in the main text shows the comparison of the experiments with these numerical simulations. We find good qualitative agreement with this small 2D coupled-chain numerical model.

In a one-dimensional system, states of the form $|11001100\dots\rangle$ (which the initial states in the experiment attempt to emulate) would be completely frozen in the limit of infinite V/t , since the Hamiltonian in that limit conserves the number of bonds ($\sum_x \hat{n}_x \hat{n}_{x+1}$). For a large but finite V , moving a single atom (and hence breaking a bond) costs an energy V . However, in the coupled-chain $t-V$ model with isotropic interaction, breaking a bond now costs up to $3V$ for the idealized initial charge density wave state. We thus expect the 2D system to have slower relaxation rate compared to a 1D system with the same interaction strength, in that limit.

To verify this, we perform additional numerical simulations on a single chain of 21 atoms. Similarly to our 2D simulation, we sample 1×19 arrays from the experimental snapshots at $t = 0$ and add empty sites at the ends. We find that the atoms spread quicker than they do in the ladder geometry and have worse agreement with the experimental results. Fig. S4 shows a comparison between the 1D and 2D coupled-chain numerical simulations and the experimental data. This comparison highlights the importance of the interchain interactions in order to fully understand our system.

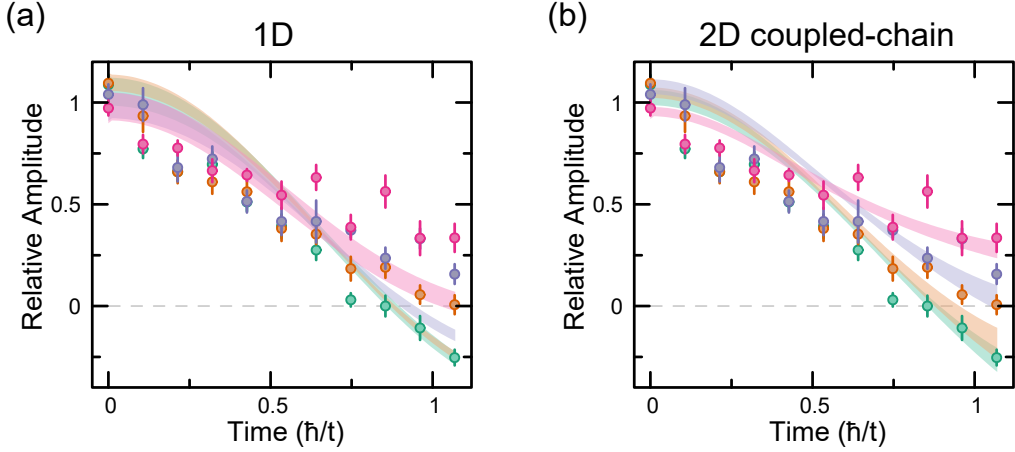


FIG. S4. **Role of interchain couplings in slowing down charge density wave relaxation.** Numerical simulations of a $t - V$ model with tunneling t along only one direction and isotropic nearest-neighbor interactions V . (a) Fitted relative sinusoid amplitude to observed (circles) and calculated quench dynamics of 1×21 systems (shaded regions). The colors represent the different interaction strengths $V/t = [0$ (green), 0.8 (orange), 1.6 (purple), 2.9 (pink)] explored in the experiment. (b) Same comparison as in (a) but for calculations done on 2×11 systems. This is Fig. 4d of the main text.